THE ASTROPHYSICAL JOURNAL, 426:669–687, 1994 May 10

MAGNETOSPHERIC ACCRETION MODELS FOR T TAURI STARS. I. BALMER LINE PROFILES WITHOUT ROTATION

LEE HARTMANN[1] AND ROBERT HEWETT
Harvard-Smithsonian Center for Astrophysics, Mail Stop 15, 60 Garden Street, Cambridge, MA 02138
AND
NURIA CALVET[1,2]
Centro de Investigaciones de Astronomia, Ap. Postal 264 Mérida 5101-A, Venezuela
Received 1993 August 12; accepted 1993 November 15

ABSTRACT

We argue that the strong emission lines of T Tauri stars are generally produced in infalling envelopes. Simple models of infall constrained to a dipolar magnetic field geometry explain many peculiarities of observed line profiles that are difficult, if not impossible, to reproduce with wind models. Radiative transfer effects explain why certain lines can appear quite symmetric while other lines simultaneously exhibit inverse P Cygni profiles, without recourse to complicated velocity fields. The success of the infall models in accounting for qualitative features of observed line profiles supports the proposal that stellar magnetospheres disrupt disk accretion in T Tauri stars, that true boundary layers are not usually present in T Tauri stars, and that the observed "blue veiling" emission arises from the base of the magnetospheric accretion column.

Subject headings: accretion, accretion disks — line: profiles — stars: pre–main-sequence

1. INTRODUCTION

The general success of circumstellar disk models in explaining the common infrared excess emission of T Tauri stars (Lynden-Bell & Pringle 1974; Rucinski 1985; Adams, Lada, & Shu 1987; Bertout 1987; Kenyon & Hartmann 1987; Bertout, Basri, & Bouvier 1988; Basri & Bertout 1989) supports the idea that a substantial fraction of the mass of a typical low-mass star is accreted through a disk (Mercer-Smith et al. 1984; Hartmann & Kenyon 1990). The optical and ultraviolet excess emission observed in many T Tauri stars is conventionally thought to arise from the boundary layer between the slowly rotating star and Keplerian disk (Lynden-Bell & Pringle 1974; Bertout et al. 1988; Basri & Bertout 1989; Hartigan et al. 1991; Bouvier & Bertout 1992). The identification of boundary layer emission is important, because the boundary layer is the region where material ultimately accretes onto the star from the disk and can therefore be used to estimate mass inflow rates.

However, certain observations are difficult to explain with the standard disk-boundary layer model. "Hot spots" inferred from photometric monitoring led Bertout et al. (1988 to suggest that boundary layer accretion could be disrupted by stellar magnetic fields; recent work suggests that such spots are common (Bouvier et al. 1993). The simple boundary layer picture suggests that the central T Tauri star should spin up as high angular momentum material is accreted, despite the fact that T Tauri stars are generally slow rotators (Vogel & Kuhi 1981; Bouvier et al. 1986; Hartmann et al. 1986; Hartmann & Stauffer 1989). In principle, stellar winds can carry off large amounts of angular momentum, but it is difficult to reconcile the required stellar wind angular momentum loss with the absence of much angular momentum loss during contraction to the main sequence (Hartmann 1991). Moreover, recent observations indicate that T Tauri stars with accretion disks near the star rotate more slowly, not faster, than T Tauri stars without inner disks (Bouvier et al. 1993; Edwards et al. 1993), a result which seems to implicate disks rather than stellar winds in the spin-down process.

It is also difficult to explain the inverse P Cygni profiles observed in many T Tauri stars (Walker 1972; Appenzeller & Wolf 1977; Bertout et al. 1977; Wolf et al. 1977; Appenzeller, Mundt, & Wolf 1978; Edwards 1979; Mundt 1979; Krautter, Appenzeller, & Jankovics 1990; Lamzin 1989) with the simple boundary layer model. The observations indicate large infall velocities, which seem to imply the gravitational acceleration of material from large distances above the stellar photosphere, inconsistent by orders of magnitude with the small radial velocities predicted by boundary layer models. With improved observational techniques, the evidence for frequent infall is accumulating (Edwards et al. 1994).

These observations could be explained with a quite different picture of T Tauri accretion, in which material falls onto the central star along extended stellar magnetic field lines (Camenzind 1990; Königl 1991; Hartmann 1991; Calvet & Hartmann 1992, hereafter CH). In this model, the infalling material attains nearly free-fall velocities, and so can explain the observed large widths of the line profiles. In addition, the infalling material will shock and radiate away its kinetic energy near the stellar surface, producing a hot continuum in the absence of a true boundary layer. Departures from axisymmetry could then provide an explanation of the photometric hot spots. If the magnetospheric model is correct, then the optical line profiles of T Tauri stars directly exhibit the final accretion of matter by solar-type stars, as originally proposed by Walker (1972) and Appenzeller &.Wolf (1977). Analysis of the line

[1] Visiting Astronomer, Kitt Peak National Observatory, operated by the National Optical Astronomy Observatory under contract to the National Science Foundation.
[2] Also Grup d'Astrofisica de la Societat Catalana de Fisica, Institut d'Estudis Catalans.

profiles can help constrain mass accretion rates for T Tauri stars, the size of magnetosphere, and the large-scale geometry of the magnetic field.

In a recent paper (CH), we used a schematic treatment to show that the magnetospheric model naturally explains the large infall velocities observed in many T Tauri stars and can potentially explain many peculiarities of permitted line profiles which are difficult, if not impossible, to explain with stellar wind or boundary-layer wind models (Calvet et al. 1992). In this paper we present further tests of the magnetospheric hypothesis, using dipole field geometry and improved radiative transfer methods. The new calculations result in line profiles with more centrally peaked emission than in CH, in better agreement with some observations. In addition, the adoption of a more realistic geometry provides better predictions of velocity shifts and better constraints on the observability of redshifted absorption.

Our results indicate that magnetospheric accretion is probably responsible for the Balmer emission-line profiles observed in BP Tau and UY Aur. Beyond this specific comparison, the calculated line profiles should be of use in testing the general validity of the magnetospheric accretion for a larger sample of T Tauri stars, such as the extensive survey of T Tauri line profiles being carried out by Edwards et al. (1993b).

2. MODEL CALCULATIONS

2.1. *Magnetospheric Model*

Our basic model is that of accretion from a disk onto a T Tauri star in which the accretion is controlled by a dipole stellar magnetic field (Fig. 1). The magnetic field is assumed to be so strong that it is undistorted by the inflow. We further assume that the gas pressure is sufficiently low that material freely falls onto the star, where the gas shocks and dissipates the accretion energy by blackbody radiation.

We adopt a coordinate system in which z is the polar axis of symmetry, r is the radial distance from the center of the star, and θ is the angle the radial vector makes with the z-axis. We further define $\boldsymbol{R}$ to be the vector projection of r onto the plane $z = 0$. Axisymmetric steady flow is assumed. For simplicity we adopt a dipole magnetic field structure, with streamlines given by

$$r = r_m \sin^2 \theta \,, \tag{1}$$

(cf. Ghosh, Lamb, & Pethick 1977), where the position $r = r_m$ corresponds to $\theta = \pi/2$. In reality, the pressure of the disk is likely to produce departures from dipole geometry in the magnetic field near the disk, pinching the magnetic field more than in the simple dipole formula (Camenzind 1990; Spruit & Taam 1990), but the predicted field structure is uncertain and so we neglect this complication.

Assuming that the (poloidal) magnetic field is undistorted and the flow is coupled to the field, the poloidal velocity $\boldsymbol{v}_p$ is parallel to the field lines,

$$\boldsymbol{v}_p = -v_p \left[\frac{3y^{1/2}(1-y)^{1/2}\hat{R} + (2-3y)\hat{z}}{(4-3y)^{1/2}} \right] \tag{2}$$

(cf. Calvet & Hartmann 1992), where $y = r/r_m = \sin^2 \theta$.

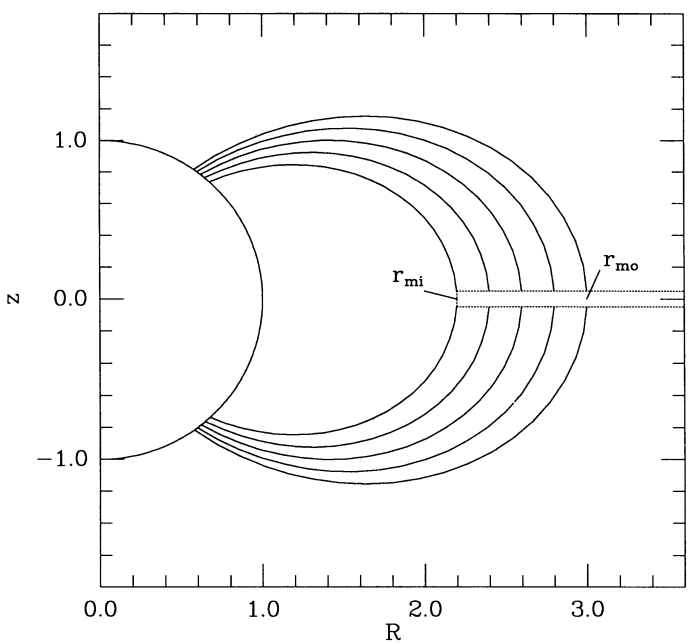

FIG. 1.—The adopted axisymmetric magnetospheric geometry shown in a poloidal plane. The circle denotes the stellar photosphere, while the dotted lines denote the disk, which is assumed to be opaque and to extend to the innermost field line, as shown. The (purely) poloidal magnetic field lines are dipolar.

Since most T Tauri stars are slowly rotating (Vogel & Kuhi 1981; Bouvier et al. 1986; Hartmann et al. 1986; Hartmann & Stauffer 1989), we initially neglect rotation, which will be considered in a subsequent paper (Daugherty et al. 1994). With no rotation, the highly supersonic flow exhibits nearly ballistic motion (Ghosh, Lamb, & Pethick 1977). We expect the velocities of the flow near the disk to be small, so the adopted velocity field corresponds to ballistic steady poloidal infall from rest at a specified radius r_m,

$$v_p = \left[\frac{2GM}{R_*}\left(\frac{R_*}{r} - \frac{R_*}{r_m}\right)\right]^{1/2} . \tag{3}$$

A poloidal section of the geometry adopted is shown in Figure 1. The infalling matter is contained within two field lines which intersect the disk at distances r_{mo} for the outermost field line and r_{mi} for the innermost field line. These field lines intersect the stellar surface at latitudes $\sin^2 \theta_{o,i} = R_*/r_{mo,i}$. Flow velocities within these limiting field lines are determined from equation (1), using the appropriate value of r_m for each field line.

The gas density is determined using the ideal MHD result for axisymmetric steady flow,

$$\rho = \eta B_p / v_p , \tag{4}$$

(cf. Mestel 1961), where η is a constant along a given field line. This equation states that the steady mass flux is confined to magnetic flux tubes. Using the magnetic field components in the Rz plane,

$$B_R = \frac{3m \sin\theta \cos\theta}{r^3} , \tag{5}$$

$$B_z = \frac{m(3\cos^2\theta - 1)}{r^3} , \tag{6}$$

where m is the magnetic moment, one can show that

$$\rho = \frac{\eta m}{r^3} \frac{(4 - 3y)^{1/2}}{(2GM/R)^{1/2}(R_*/r - R_*/r_m)^{1/2}} . \tag{7}$$

The density can be related to the total mass flux onto the star,

$$\dot{M} = 2 \int_{\theta_i}^{\theta_o} 2\pi R_*^2 \sin\theta \, d\theta \, \rho(R_*) v_r(R_*) , \tag{8}$$

where θ_o and θ_i correspond to the limiting angles of equation (1) and the factor of 2 in front accounts for accretion into rings in both hemispheres. For simplicity we assume that η is a constant over *all* field lines. This assumption is not clearly justified, but there seems to be no reason to adopt a more complicated structure; the actual value will be controlled by the processes in the disk by which matter gets loaded onto the field lines, which are not well understood. With this assumption, after some manipulation we find

$$\rho = \frac{\dot{M} R_*}{4\pi(R_*/r_{mi} - R_*/r_{mo})} \frac{r^{-5/2}}{(2GM)^{1/2}} \frac{(4 - 3y)^{1/2}}{(1 - y)^{1/2}} . \tag{9}$$

For typical parameters the velocity of the infalling gas is several hundred km s^{-1} immediately above the stellar surface. The infalling gas will be decelerated in a strong shock and heated to $\sim 10^6$ K. The X-ray radiation produced in the shock will be absorbed very close to the shock and reprocessed in optically thick regions into optical and ultraviolet radiation (see Königl 1991). We assume that all of the free-fall kinetic energy is thermalized in the radiating layer and approximate the accretion luminosity by

$$L_r = \frac{GM\dot{M}}{R_*}\left[1 - \frac{2R_*}{(r_{mo} + r_{mi})}\right] , \tag{10}$$

which agrees to within a few percent of the exact relation obtained using equations (3) and (9).

We assume that this accretion luminosity is radiated as blackbody emission from the base of the magnetosphere, i.e., between θ_o and θ_i. Thus, the temperature of the hot ring is related to the luminosity by

$$L_r = 2 \int_{\theta_i}^{\theta_o} 2\pi R_*^2 \sin\theta \, d\theta \, \sigma T_r^4 , \tag{11}$$

so that

$$T_r^4 = L_r / [4\pi R_*^2 \sigma(\cos\theta_i - \cos\theta_o)] , \tag{12}$$

where equation (1) gives the relation between the latitude limits and the maximum radii of the outer field lines r_{mo} and r_{mi}.

2.2. *Radiative Transfer Methods*

The emission envelopes of T Tauri stars are estimated to exhibit temperatures $\lesssim 10^4$ K (Natta, Giovanardi, & Palla 1988; Hartmann et al. 1990). Since line profile widths and line shifts are typically several tens to hundreds of km s^{-1} (cf. Hartmann 1982; Mundt 1984), the flows are highly supersonic. Moreover, the required infall velocities are $\sim$200–300 km s^{-1} (Calvet & Hartmann 1992). Under these conditions the Sobolev method can be a useful approximation to obtain the line source funtions.

The detailed method we use was developed by Rybicki & Hummer (1978), and was previously used to investigate infalling envelopes of T Tauri stars by Bertout (1977, 1979a, b) and Bastian (1982). We therefore limit our discussion to a brief outline of the

general procedure, giving details important for our specific application. Further description of the theory can be found in the above references.

An atom emitting a specific line transition interacts only with other atoms having similar velocities along the line of sight. In the case of supersonically moving atmospheres, the Doppler shifts that occur are large compared with the natural (thermal) line widths, an atom emitting in a specific transition interacts with other atoms having a limited range of relative velocities, which occupy a small volume of the atmosphere. In the limit of large velocity gradients, these volumes of atoms that can interact or are the resonant with a given point are very thin. The Sobolev approximation assumes that the volumes are so thin that physical properties of the medium remain constant across the resonant layers, and that these layers are in effect "resonant surfaces." The radiative transfer methods thus assume that the solutions are dominated by local terms plus interactions with a (few) resonant surface(s).

Specifically, if at point $\boldsymbol{r}$ the velocity is $\boldsymbol{v}$, the distance vector $\boldsymbol{r}'$ of the resonant or "common point" (CP) surface is given by (Rybicki & Hummer 1978)

$$(\boldsymbol{r} - \boldsymbol{r}') \cdot [\boldsymbol{v}(\boldsymbol{r}) - \boldsymbol{v}(\boldsymbol{r}')] = 0 \, . \tag{13}$$

The radiative transfer calculations take into account interactions between all such common point surfaces, and the radiation field of the star plus its hot accretion ring (see § 2.1).

For a two-level atom in complete redistribution, the line source function S is

$$S(\boldsymbol{r}) = [1 - \epsilon(\boldsymbol{r})]\bar{J}(\boldsymbol{r}) + \epsilon(\boldsymbol{r})B(\boldsymbol{r}) \, , \tag{14}$$

where B is the local Planck function and ϵ is the ratio of the collisional to total de-excitation rates from the upper level,

$$\epsilon = \frac{C_{ul} N_e(\boldsymbol{r})}{C_{ul} N_e(\boldsymbol{r}) + A_{ul}} \, , \tag{15}$$

ignoring stimulated emission. Here C_{ul} is the collision rate per electron, N_e is the electron density, and A_{ul} is the Einstein coefficient of the transition. $\bar{J}$ is the integrated mean intensity of the line,

$$\bar{J} = \frac{1}{4\pi} \int d\Omega(\boldsymbol{n}) \int dv \, \phi\left[v - \frac{v_0}{c} \boldsymbol{n} \cdot \boldsymbol{v}(\boldsymbol{r})\right] I(\boldsymbol{r}, \boldsymbol{n}, v) \, , \tag{16}$$

where $I(\boldsymbol{r}, \boldsymbol{n}, v)$ is the specific intensity at $\boldsymbol{r}$ in a direction defined by the unit vector $\boldsymbol{n}$ and at frequency v; the line center frequency is v_0 and c is the speed of light. The first integral is taken over all solid angles Ω around $\boldsymbol{n}$.

The mean intensity is related to the source function by

$$\bar{J} = [1 - \beta(\boldsymbol{r})]S(\boldsymbol{r}) + \beta_{c*}(\boldsymbol{r})I_* + \beta_{cr}(\boldsymbol{r})I_r + F(\boldsymbol{r}) \, , \tag{17}$$

where

$$\beta(\boldsymbol{r}) = \frac{1}{4\pi} \int d\Omega(\boldsymbol{n}) \frac{1 - e^{-\tau(\boldsymbol{r}, \boldsymbol{n})}}{\tau(\boldsymbol{r}, \boldsymbol{n})} \, , \tag{18}$$

$$\beta_{c*}(\boldsymbol{r}) = \frac{1}{4\pi} \int_* d\Omega(\boldsymbol{n}) \frac{1 - e^{-\tau(\boldsymbol{r}, \boldsymbol{n})}}{\tau(\boldsymbol{r}, \boldsymbol{n})} e^{-\sum_{j=1}^{N} \tau(\boldsymbol{r}_j, \boldsymbol{n})} \, , \tag{19}$$

$$\beta_{cr}(\boldsymbol{r}) = \frac{1}{4\pi} \int_r d\Omega(\boldsymbol{n}) \frac{1 - e^{-\tau(\boldsymbol{r}, \boldsymbol{n})}}{\tau(\boldsymbol{r}, \boldsymbol{n})} e^{-\sum_{j=1}^{N} \tau(\boldsymbol{r}_j, \boldsymbol{n})} \, , \tag{20}$$

$$F(\boldsymbol{r}) = \frac{1}{4\pi} \int d\Omega(\boldsymbol{n}) \frac{1 - e^{-\tau(\boldsymbol{r}, \boldsymbol{n})}}{\tau(\boldsymbol{r}, \boldsymbol{n})} \sum_{j=1}^{N} S(\boldsymbol{r}_j)[1 - e^{-\tau(\boldsymbol{r}_j, \boldsymbol{n})}] e^{-\sum_{i=1}^{j-1} \tau(\boldsymbol{r}_i, \boldsymbol{n})} \, . \tag{21}$$

The solid angle integral for β_{c*} is taken over the stellar photosphere, which is assumed to have a (constant) specific intensity I_*, and for β_{cr} it is taken over the hot ring at the base of the magnetosphere (§ 2.1), which is assumed to have a (constant) specific intensity I_r. The specific intensities are taken as blackbodies at the photospheric effective temperature and at T_r, defined by equation (12). The terms

$$e^{-\sum_{j=1}^{N} \tau(\boldsymbol{r}_j, \boldsymbol{n})}$$

account for extinction of light sources by N intervening CP surfaces.

The optical depths are defined by

$$\tau(\boldsymbol{r}_i, n) = k(\boldsymbol{r}_i, n) \frac{c}{v_0} \frac{1}{|Q(\boldsymbol{r}_i, \boldsymbol{n})|} \, . \tag{22}$$

Q is defined by

$$Q(\boldsymbol{r}_i, \boldsymbol{n}) = \frac{dv_n(\boldsymbol{r}_i)}{dl_n} \, , \tag{23}$$

where $v_n = \boldsymbol{v} \cdot \boldsymbol{n}$, and dl_n is the length element in the direction of $\boldsymbol{n}$. The line opacity is

$$k(\boldsymbol{r}_i, \boldsymbol{n}) = \frac{\pi e^2}{mc} f N_l(\boldsymbol{r}_i)\left[1 - \frac{g_l N_u(\boldsymbol{r}_i)}{g_u N_l(\boldsymbol{r}_i)}\right]. \tag{24}$$

where N_l and N_u are the populations of the lower and upper level, respectively, and other terms have the usual meaning. By combining equations (14) and (17) we can solve for the line source function in the two-level atom approximation, provided the lower level population is known. As discussed in § 2.3 below, we use approximate methods to find the $n = 2$ level populations to calculate Balmer lines. In principle, these equations can and should be solved iteratively for a multilevel atom. We retain the two-level atom approximation for an initial exploration of the plausibility of the model.

Even adopting a two-level atom, the solutions must be obtained iteratively because the term F makes the problem nonlocal. As the initial guess we assume that $F = 0$ and calculate the corresponding source function. Then a new value of S is calculated using the old value in the term for F. This procedure converges rapidly after only two iterations, because F generally never contributes very much to the source function.

At each point in the atmosphere where we wish to find the source function, the angle integrals are taken using a finite number of lines of sight. The lines of sight are determined in a coordinate system θ', ϕ', where $\theta' = 0$ corresponds to the center of the stellar disk. The lines of sight were sampled uniformly in two regions, $\theta' < \theta'(R_*)$ and $\theta' > \theta'(R_*)$, corresponding to lines of sight intersection or missing the stellar disk. We required the same number of angle samples on the star for all positions in the magnetosphere, which enabled us to ensure that we were sampling the stellar radiation field adequately. We assume that the disk exterior to r_{mi} (Fig. 1) is opaque and black at optical frequencies.

The emergent line profiles were calculated by summing up the emission from the resonant surfaces at a given frequency,

$$F_v = \sum_k \sum_l r_k'' \, dr_k' \, d\phi_l''\left[\sum_j^N S_j(r_k'', \phi_k'') e^{-\sum_{i=1}^{j-1} \tau(r_i, m)}(1 - e^{-\tau(r_j, m)}) + I_{c*,r} \, e^{-\sum_{j=1}^{N} \tau(r_j, m)}\right]. \tag{25}$$

In this expression (r'', ϕ'') is a polar coordinate system centered on the stellar disk and perpendicular to the line of sight. The sums are taken over CP surfaces j, while the sums over i correspond to CP surfaces between surface j and the observer (cf. Rybicki & Hummer 1978). If the line of sight (direction $\boldsymbol{m}$) intersects the star, the term in I is included, with a blackbody intensity corresponding to the adopted photospheric temperature or to the hot ring temperature, depending upon which is appropriate. As in the source function calculation, we assume that the disk exterior to r_{mi} is opaque and black at optical frequencies.

2.3. *Model atoms and Ionization Calculations*

For an initial exploration we adopt the following simplified model atoms and treatment of ionization. We assume a two-level plus continuum hydrogen atom,

$$N_1 + N_2 + N_k = N_{\rm H}, \tag{26}$$

where N_n is the population of the n level, N_k is the proton population and $N_{\rm H}$ is the total hydrogen density. We also assume that the Lyman continuum is in radiative balance, so the ionization is controlled by photoionizations out of the Balmer continuum balancing recombinations to the $n = 2$ level (Hartmann & MacGregor 1981). The ionization equation in this case is

$$\frac{N_2}{N_k} = \frac{R_{k2}}{R_{2k}} \sim \frac{\alpha_2(T) N_e}{R_{2k}}, \tag{27}$$

where R_{k2} and R_{2k} are the recombination and photoionization rates of level $n = 2$, α_2 is the recombination coefficient to level $n = 2$, and N_e is the electron density, which we assume to have a fixed contribution from neutral metals $\alpha_M = 10^{-4}$, i.e.,

$$N_e = N_k + \alpha_M N_{\rm H}. \tag{28}$$

The ionizing radiation field is described by fixed radiation temperatures, which include a contribution from the stellar photosphere and a contribution from the accretion shock on the star, each weighted by the solid angle subtended from the given point. The assumed radiation temperatures are the photospheric effective temperature and T_r.

The statistical equilibrium equation for level $n = 1$ is solved in terms of the net radiative bracket for Lyα, which is substituted by the escape probability, given by equation (18) if multiple crossings are neglected. Then

$$\frac{N_2}{N_1} = \frac{\Omega_{12} N_e}{\Omega_{21} N_e + A_{21} \beta_{21}}, \tag{29}$$

where Ω_{nm} is the collisional cross section and A_{21} is the Einstein coefficient. Since the optical depth in Lyα is large, substitution of equation (22) in equation (18) implies that β_{21} is proportional to the population in $n = 1$, and to the solid angle average of the velocity gradient at the given point, which is independent of the density calculations.

The set of equations (26)–(29) can be solved for the unknowns N_1, N_2, N_k, and N_e, for given T and $N_{\rm H}$ and a description of the ionizing field.

The above calculations were implemented in a C++ program written by one of the authors (R. H.).

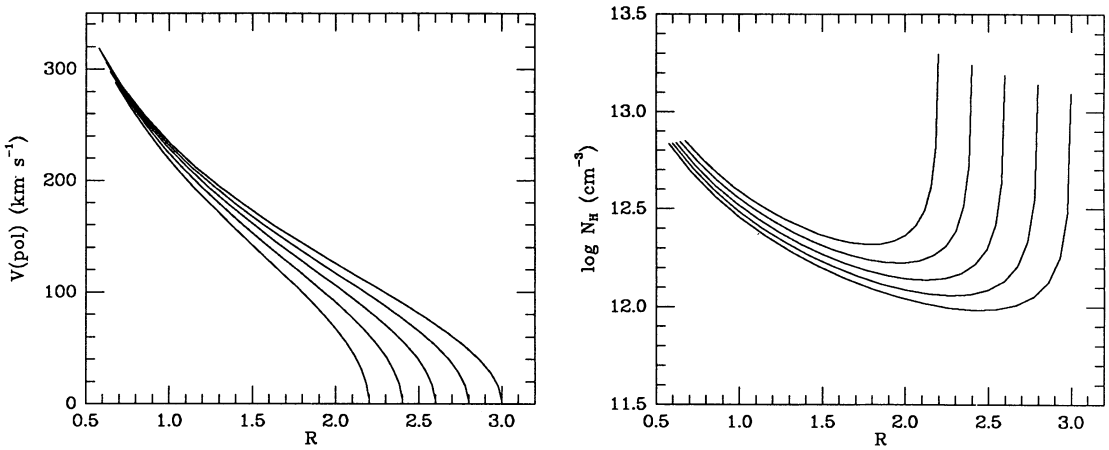

FIG. 2.—Density and velocity structure of all models as a function of cylindrical radius R (cf. Fig. 1). The lines denote the variation of properties along the field lines denoted in Fig. 1.

3. RESULTS

3.1. *Basic Parameters*

For all cases we assume a typical T Tauri stellar mass and radius of $M_* = 0.8\ M_\odot$ and $R_* = 2\ R_\odot$, and an effective temperature of the (undisturbed) photosphere of 4000 K. We evaluated the line source functions on a grid sampled at 20 points uniformly along five individual field lines within the magnetosphere to make interpolation simpler. The angle integrals were performed with 40 angle points each in θ' and ϕ', with half of the sampling covering the projected stellar disk. The line profiles were calculated using 40 projected radius points r_k'' on the stellar disk and another 60 projected radius points exterior to the disk, and 100 angle points ϕ''.

As shown in Figure 1, we adopt $r_{mo} = 2.2\ R_*$ and $r_{mi} = 3.0\ R_*$. These limits correspond to the portion of the magnetosphere containing the infalling material; other stellar magnetic field lines might penetrate the disk at larger radii (cf. Königl 1991). We have chosen a small magnetosphere for our preliminary exploration to speed up the computation times. With these parameters, the hot region at the base of the magnetosphere covers $\sim 8\%$ of the stellar surface in each hemisphere, which is reasonably consistent with observational estimates (Basri & Bertout 1989; Hartigan et al. 1991). Results for a larger magnetosphere are considered in § 3.5.

In Figure 2 we show the velocity field and hydrogen density distribution along several field lines (cf. eqs. [3] and [9]) within the standard magnetosphere for an adopted infall rate of $\dot{M} = 10^{-7}\ M_\odot\ \mathrm{yr}^{-1}$, typical of estimated T Tauri accretion rates (Basri & Bertout 1989). The qualitative nature of the density distribution is determined by mass conservation in steady flow. The density rises near the disk as the velocity decreases; close to the star, the narrowing of the flux tube area causes the density to similarly increase for nearly constant infall velocity (eq. [9]).

Figure 3 displays the CP surfaces for a typical point in the magnetosphere. The point is assumed to be in the x-z plane, and orthogonal three planar projections of the surfaces are shown. Many more rays were used to illustrate the surface than are actually used in the calculation of the nonlocal term F, and so the result is somewhat noisy (§ 3.3). However, the approximate calculation of

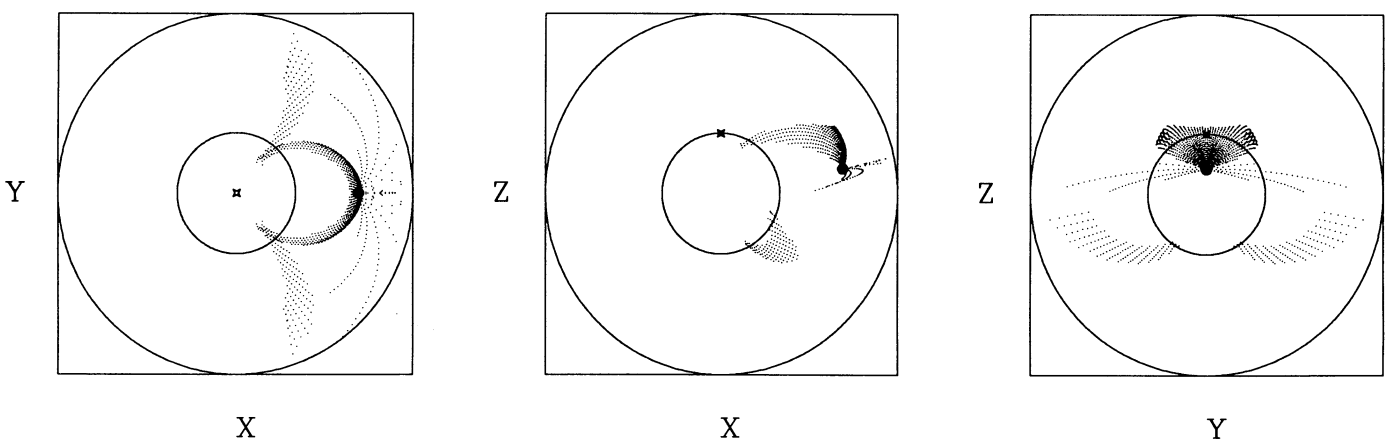

FIG. 3.—Three orthogonal projections of the common point (CP) surfaces in the magnetosphere as seen from a typical point, marked by a large dot. The x-y plane contains the disk and z is the rotational axis. The inner circle represents the stellar disk, with the open star marking the north pole of the stellar photosphere; the outer circle represents the outermost limit of the magnetosphere. The leftmost panel is a view from polar directions; the large dot is the position of observation, at $x = 2.07$, $y = 0$, $z = 0.41$. The middle and right panels are views of the CP surfaces in the disk plane; the middle panel corresponds to viewing along the y-axis, while the right panel is a view along the x-axis.

F does not strongly affect our results, because the other terms in equation (17) for the mean intensity are generally (but not always) much larger.

3.2. *Isothermal Atmosphere: Optically Thin Profiles*

We start by examining a particularly simple case, in which the line source function is in LTE, i.e., $S = B$, and the line has a constant fractional abundance and is optically thin. For concreteness we adopt the atomic parameters of the [O I] λ6300 forbidden line. We assume that all of the oxygen is neutral with the constant adopted envelope temperature 6500 K. The assumption of LTE should be reasonable for [O I] because the electron densities are sufficiently high (Fig. 2), placing the 6300 Å line in the high-density limit (Osterbrock 1974). We neglect hot ring emission and assume that the stellar photosphere has a uniform surface temperature.

The profiles calculated for this case are shown in the left-hand side of Figure 4. The emission is generally strongly peaked near line center. The low-velocity emission peak is produced in the part of the magnetosphere near the disk, where the infall velocity is small. In this region the density is high because of mass conservation (Fig. 2), and this leads to a large emission measure at low velocities.

At low inclinations i there is a strong asymmetry in the line profile, with much larger emission on the negative velocity side of line center, because of the occultation of the receding flow by the opaque disk. Our magnetospheric region begins a finite distance above the disk plane (see Fig. 1), where the gas has already acquired a velocity ~ 10 km s^{-1}; therefore, at small i, there is no material exactly at zero velocity and so the emission drops at line center. The subsidiary peaks in the $i = 10°$ case are apparently produced by the variation of the emission measure relative to the line-of-sight velocity. Material in the near-hemisphere first approaches the observer and then recedes as it falls toward the star, and the region where the projected velocity gradient changes sign corresponds to the peaks.

The line width is small at low inclinations because the high-velocity infalling material near the star, moves obliquely to the line of sight (Fig. 1). At larger inclinations, the high-velocity portion of the flow is more nearly along the line of sight, and so the velocity width of the line increases. At nearly equator-on inclinations (e.g., $i = 75°$), the peak line emission moves toward zero velocity. This occurs because the low-velocity emission arises from near the disk (see above), and viewed nearly in the disk plane the motion of this material is essentially perpendicular to the line of sight (cf. Fig. 1).

3.3. *Isothermal Atmosphere: Optically Thick Profiles*

We next consider profiles of the Hα line in the same isothermal magnetosphere as discussed previously. The results are shown in the right column of Figure 4. The emission profiles generally have the same qualitative features as the optically thin profiles.

Figure 5 shows that the strong central emission peak is due to a large source function ($\approx J$) in the outer regions of the magnetosphere. The source function rises because the line is more thermalized at large distances, due to a combination of large $n = 2$ population and low velocity gradients, which decrease the escape probability and increase ϵ. The calculation of the mean intensity $\bar{J} \approx S$ shows some inaccuracy for the outermost field line due to the increasing importance of the nonlocal interaction term F, which is somewhat noisy.

These calculations show a qualitative difference from the previous isothermal results of CH in the strength of the central peak. The reasons for this difference lie in the treatment of the source function and the adopted geometry. In CH, an approximate escape probability method was used which included nonlocal effects with a finite thermal/turbulent velocity. This meant that the source function decreased toward the edges of the magnetosphere. Furthermore, CH used an unrealistic radial cone geometry, in which the low-velocity material was located at the end of a cone rather than at the disk. The combination of these effects meant that the low-velocity material had a smaller source function, and thus the central peak was much less pronounced; in fact, the low-velocity portion of the line profile generally exhibited absorption rather than emission. In contrast, the present calculations show no central absorption, because of the essentially local aspect of the Sobolev approximation.

The details of all our calculations close to line center should be regarded with caution for two reasons. First, at low velocities comparable to expected thermal velocities ~ 10 km s^{-1}, the assumptions of the Sobolev approximation begin to break down and the problem becomes highly nonlocal. Second, we have neglected the effect of rotation. For a typical T Tauri star with a surface rotational velocity ~ 10 km s^{-1}, a stiff magnetosphere would cause material near the disk to be rotating at ~ 30 km s^{-1} for a magnetospheric radius $\sim 3R_*$. The effects of rotation on the line profile will be considered in a subsequent paper (Daugherty et al. 1993); however, one may note immediately that the central emission spike seen at high inclinations will be suppressed or modified by the rotation.

3.4. *Nonisothermal Atmosphere: Balmer Lines*

The optically thick line profiles shown in Figure 4 are not particularly representative of the Balmer lines of T Tauri stars (cf. Hartmann 1982; Mundt 1984; Basri et al. 1989). The emission strengths are far too large, and the profiles are too centrally peaked to adequately represent the Balmer line profiles seen in most objects. This feature of the line profile is very sensitive to a number of effects, including the temperature structure of the outer magnetosphere. The processes responsible for heating the envelopes of T Tauri stars are not well understood (CH). One possibility is that magnetic waves are excited which damp and heat the infalling gas (CH). Ohmic dissipation associated with reconnection of field lines in the star or in the differentially rotating disk might also contribute some heating (Königl 1993), along with ambipolar diffusion of partially ionized gas at the disk surface (cf. Safier 1993). Another possibility is that the radiation field of the hot material at the base of the accretion column is ultimately responsible. Although photoionization heating directly from the Lyman continuum is not possible given the large hydrogen column densities of the infalling material (CH), photoionization from the *Balmer* continuum may provide sufficient heating, a hypothesis we are currently exploring.

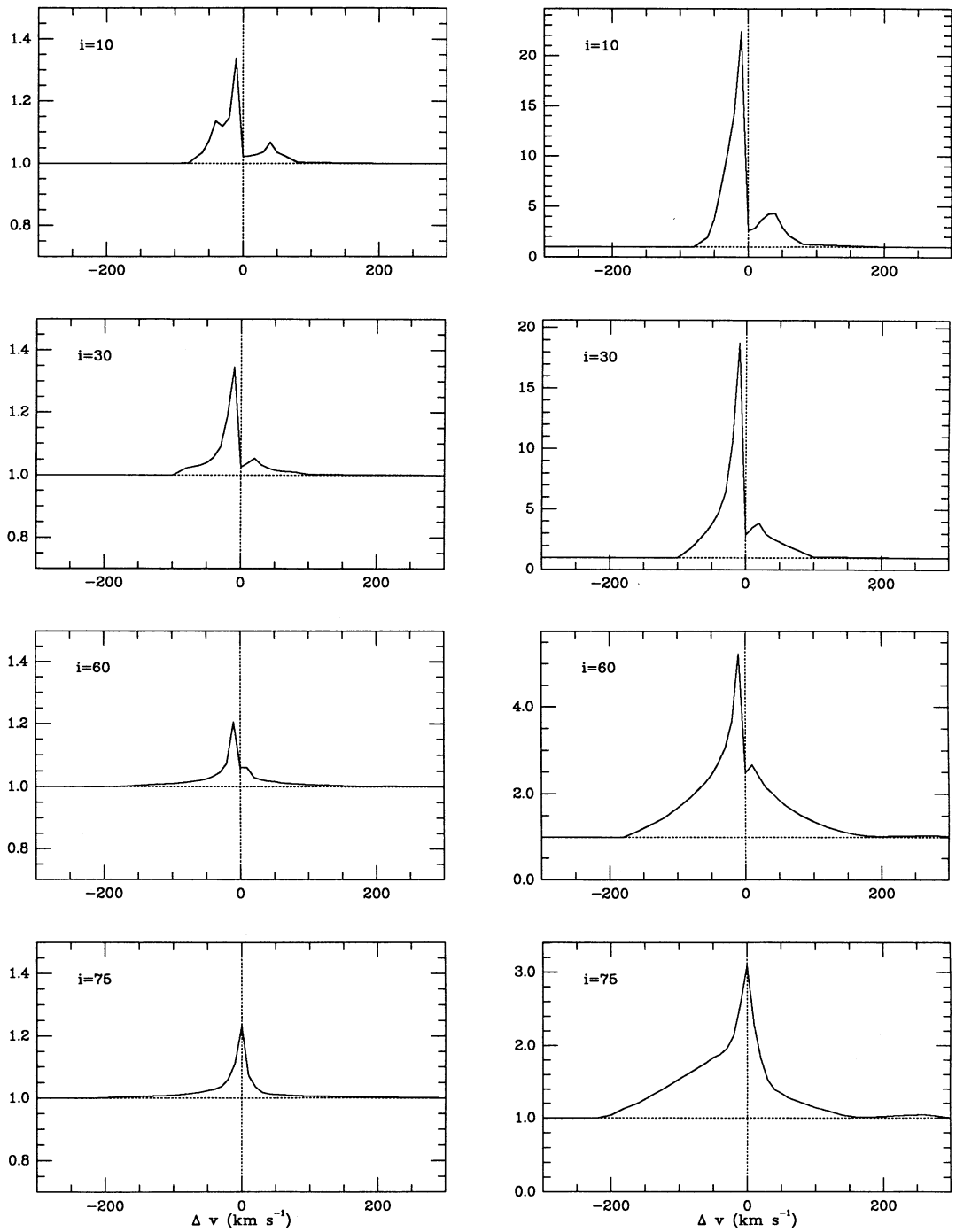

FIG. 4.—Calculations of optically thin (*left*) and optically thick (*right*) line profiles for the isothermal ($T = 8000$ K) magnetosphere (see text; Fig. 2).

For present purposes of exploring the general types of profiles produced in magnetospheric accretion, we adopt the simple temperature structure shown in Figure 6. This temperature distribution was calculated assuming a volumetric heating rate $\propto r^{-3}$ and balancing the energy input with the highly schematic radiative cooling rate used by Hartmann et al. (1982). Such a heating rate might occur for a flux of Alfvén waves generated by inhomogeneous accretion (Scheurwater & Kuijpers 1988) with a (roughly constant) damping length comparable to or larger than the magnetosphere. For present purposes the essential point is that the temperature distribution is smoothly varying and is relatively constant over most of the magnetosphere. There is a substantial decline in temperature near the disk because the magnetospheric density increases, strongly enhancing the radiative cooling. The resulting source function for Hα is essentially constant over most of the magnetosphere. The decrease in S near the disk is due to the temperature decrease; the line is essentially thermalized over the entire region and thus follows the Planck function closely. The

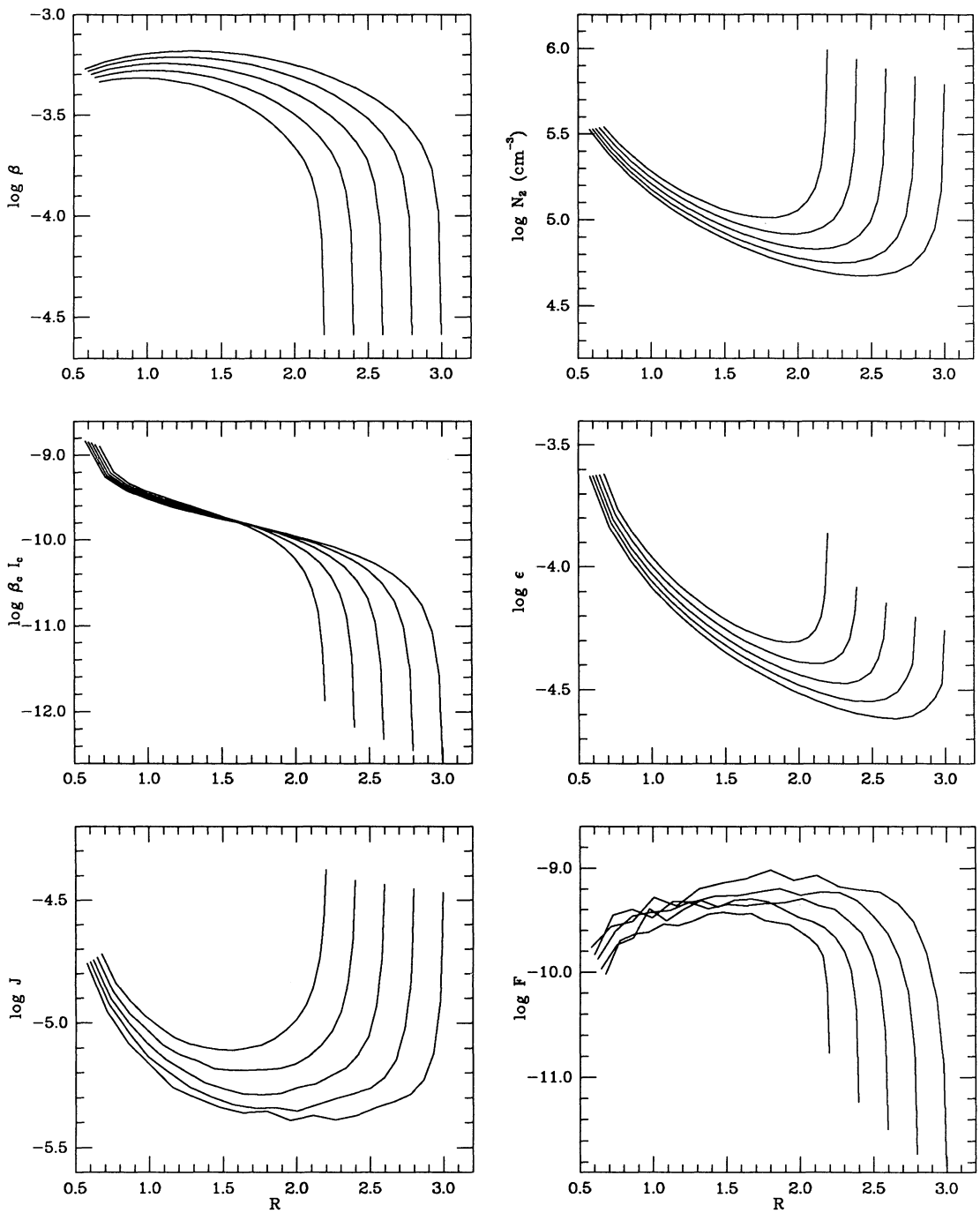

FIG. 5.—Properties of an isothermal infall model, $T = 6500$ K, for the Hα line displayed in the right-hand side of Figure 4. The lines denote quantities taken along individual field lines, as in Fig. 2.

decrease in temperature in the outer magnetosphere causes the level 2 number density to fall off dramatically (compare Fig. 6 with Fig. 5 for the isothermal case), resulting in lower Balmer line optical depths in the outer magnetosphere.

It is clear that, absent a theory for the temperature distribution, our profile calculations can be only indicative and not conclusive. We feel this approach is justified for two reasons. It is not unreasonable to suppose that gas temperatures decrease near the disk, given the enhanced radiative cooling produced by high densities in this region. Beyond this, our approach is merited if the adoption of a smooth, plausible temperature distribution results in line profiles which agree with observations, especially in aspects which are qualitatively difficult to explain with other types of models.

Figure 7 shows Hα line profiles calculated for this model. The nearly central emission peak is dramatically suppressed relative to the wings due to the declining temperature in the outer regions. At $i = 10°$, the declining temperature produces an apparent

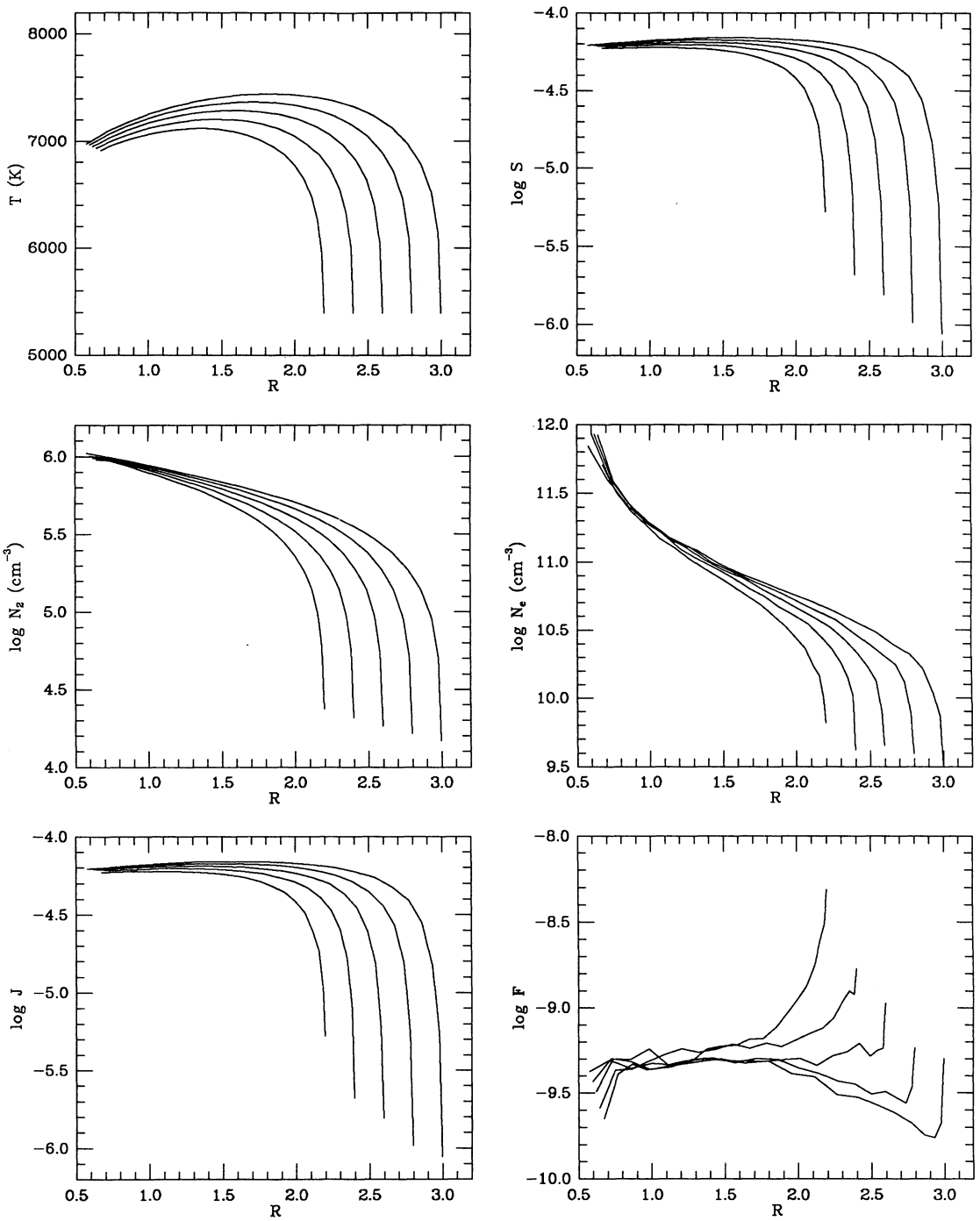

FIG. 6.—Temperature structure, Hα source function, hydrogen level 2 population, electron density, mean line intensity, and nonlocal contribution term F for the non-isothermal model (see text).

absorption reversal near line center. The overall profile shapes more nearly resemble results of CH, except that CH generally found strong absorption reversals at low velocities (as discussed above in § 3.3).

The characteristic line optical depths for Hα in this model are $\sim 10^4$. For such large values of the line optical depth, the Stark broadening wings of the line profile begin to become important, in which case the Sobolev approximation is not appropriate. In the following we therefore concentrate on calculating Hβ and Hγ, which have smaller optical depths and for which the neglect of damping wings is therefore less problematic. These calculations are performed using a crude two-level atom approximation, i.e., for Hβ the two levels are assumed to be $n = 2$ and $n = 4$, etc. The neglect of interactions between the upper levels of hydrogen is not correct, and ultimately we will develop models in which multilevel atomic models are used. We use the two-level approximation for our initial exploration of the problem, which seems justifiable since the temperature distribution in the magnetosphere is not certain.

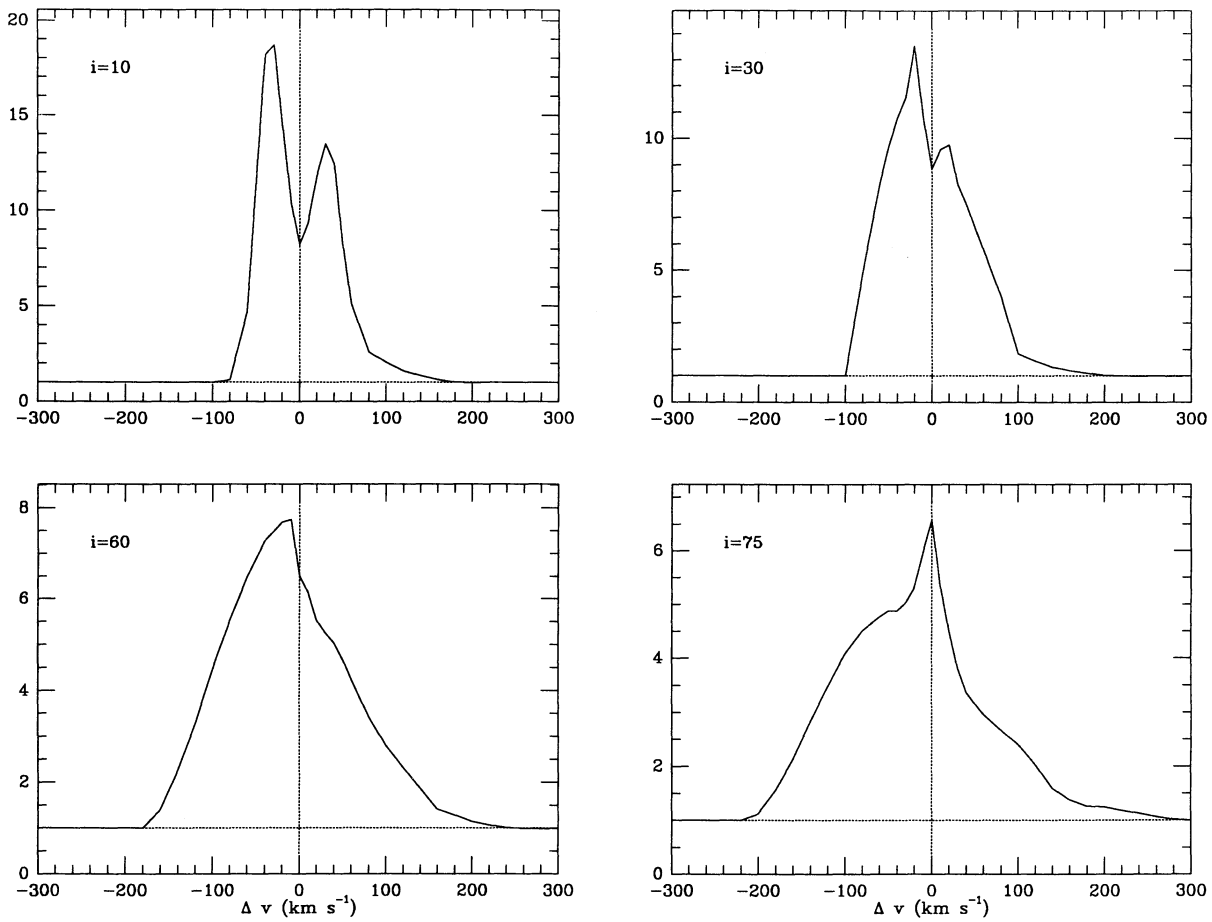

FIG. 7.—Hα profiles calculated for the model of Fig. 6

Figure 8 shows Hβ and Hγ profiles for the above model. There is no redshifted absorption feature characterizing infall. The reasons for this is that the emissivity is higher than the photospheric background. The only evidence for infall is the presence of extended *red* wings on the profile; the highest-velocity blueshifted material is occulted by the star, causing the asymmetry.

Figure 9 shows the same calculation as in Figure 8, except now the emission from the hot ring is included. For the assumed parameters, T_r in equation (12) is 7230 K. In this case redshifted absorption can be detected. The reason for this is indicated in Figure 10, which shows the Hβ source functions for the infall model with and without hot ring emission. Figure 10 shows that in both cases the Hβ source function falls below the local Planck function because it is not thermalized. The presence of a hot ring increases the line source function, due to scattering of the light of the ring; however, the source function is lower than the Planck function of the hot ring. Thus, at large inclinations, where the (optically thick) infalling gas is observed projected onto the hot ring, (see Fig. 1), line absorption is observed. At low inclinations (pole-on) the infalling gas stream is projected more onto the cool stellar photospheric background; since the infalling gas has a higher source function than the Planck function of the photosphere, this does not produce absorption.

The absorption components for the model with hot ring are much more evident in Hγ than in Hβ. As suggested by CH, this is due to the lesser thermalization in Hγ. The model provides another example of a more general result, namely, that less-thermalized lines should show redshifted absorption more prominently.

We note that in this model, the estimated Paschen continuum optical depths are of order 0.05 near Hβ and Hγ. Significantly hotter or denser models would need to include continuum processes to be self-consistent. We ignore these complications in these preliminary investigations, but point out that the infalling material might be responsible for some of the continuum emission previously identified with the "boundary layer."

CH suggested that, at low inclinations, one might observe *blueshifted* absorption if the source function at low velocities is sufficiently small, due to the fact that material near the disk is moving toward the observer (Fig. 1). We do not observe this effect in our models; however, it may be possible to produce such an effect with a much smaller source function in the outer magnetosphere than characteristic of the present models.

3.5. *Large Magnetosphere*

The choice of outer magnetospheric radius in our model affects the line profiles through the change in geometry. We do not consider much smaller magnetospheres, because in such models the infall velocity would be much smaller than observed (see below).

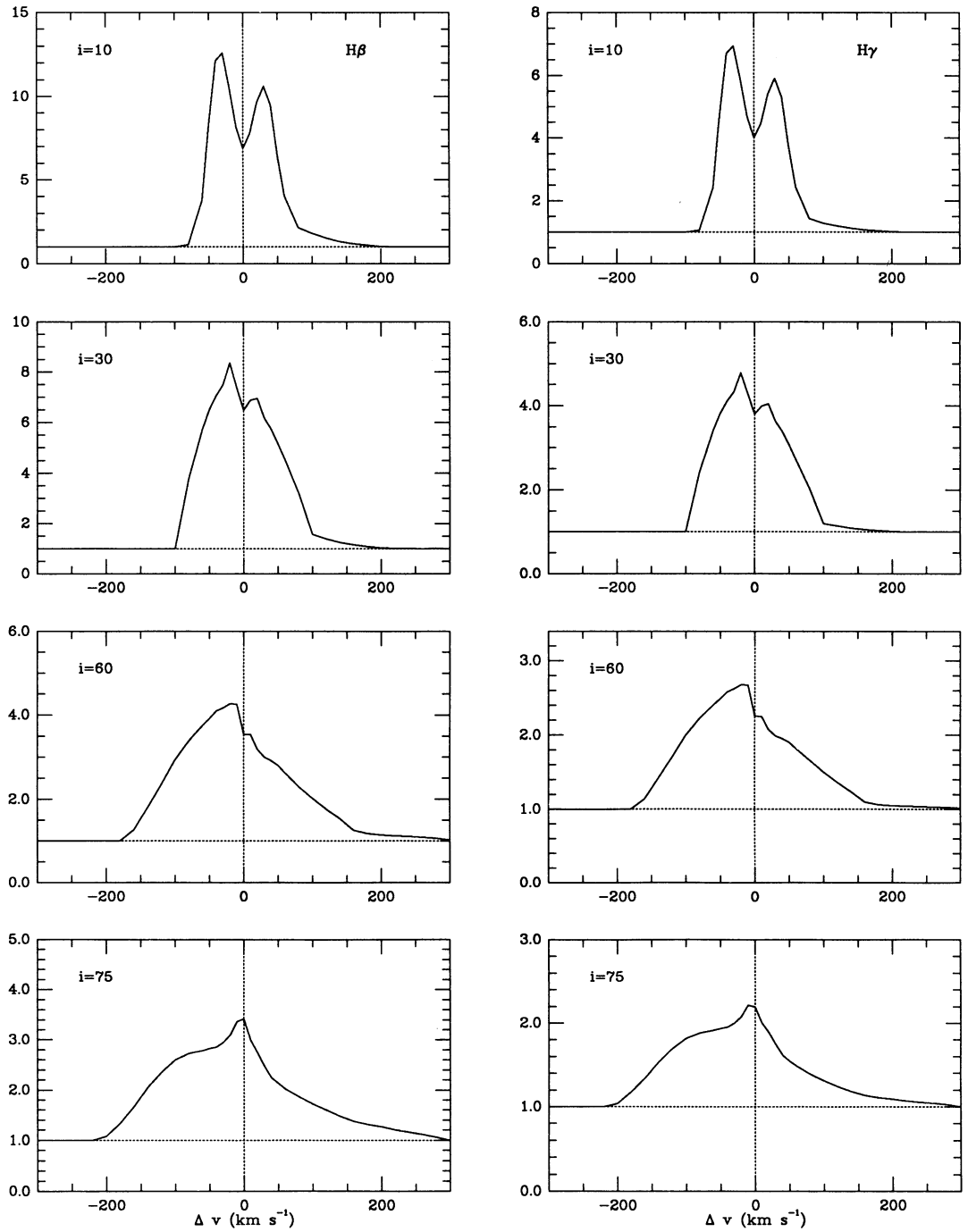

FIG. 8.—Hβ (*left*) and Hγ (*right*) line profiles for the magnetospheric model of Fig. 6, assuming no hot ring emission

We have considered a case in which r_{mi} and r_{mo} are twice as large as in the above calculations. This is motivated by the idea that the part of the magnetosphere controlling the accreting material might extend closer to the co-rotation radius (typically ~ 5–$7\ R_*$; Königl 1991). The envelope temperature was lowered, because otherwise the emission strengths would have been too large. The overall temperature structure resembles that of the previous nonisothermal cases, with nearly constant temperatures over much of the magnetosphere but a steep decline in temperature approaching the disk.

In Figure 11 we show Hα profiles for this case. The basic features of the line profile are similar to those in the previous cases, suggesting that comparison of the models with observations will not strongly constrain the maximum size of the magnetosphere. The principal difference from the smaller magnetosphere is higher velocity wings, particularly at low inclination. This is mostly due to the change in magnetosphere geometry; a larger outer radius corresponds to infall at a higher latitude on the star (cf. eq. [1]). The high latitide of infall also results in eliminating the redshifted absorption at $i = 75°$.

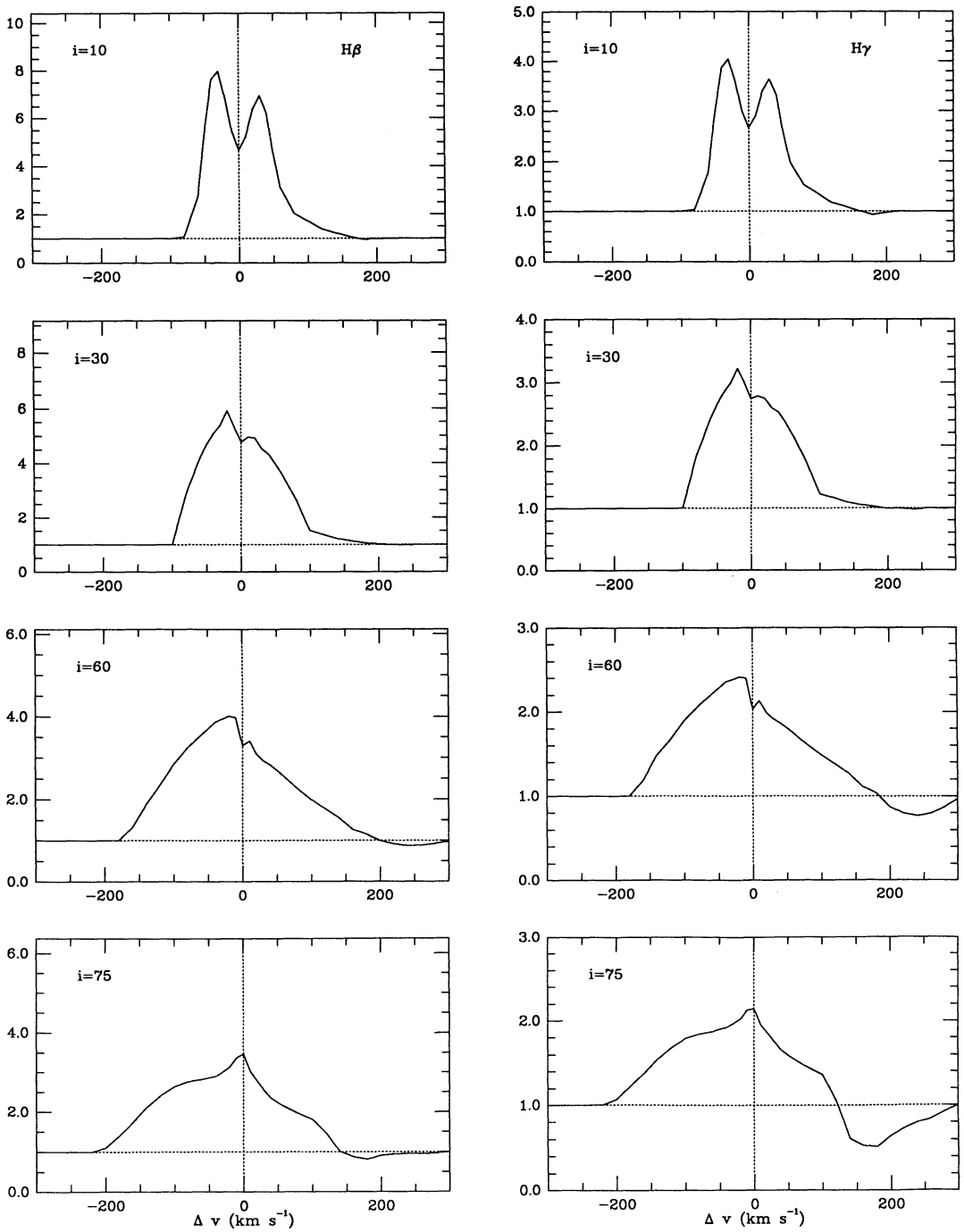

FIG. 9.—Hβ (*left*) and Hγ (*right*) line profiles for the magnetospheric model of Fig. 6, assuming hot ring emission at the base of the magnetosphere (see text)

These calculations suggest that redshifted absorption might be less frequently visible with larger magnetospheres. However, it should be kept in mind that real stellar magnetospheres are unlikely to be perfectly axially aligned dipoles, making it difficult to draw firm conclusions from the present axisymmetric models.

4. COMPARISON WITH OBSERVATIONS

For comparison with our theoretical calculations, we show a few sample line profiles of T Tauri stars which were observed with the echelle spectrograph and TI5 CCD detector on the KPNO 4 m telescope 1992 December 5–6. We used the 31 g mm^{-1}-63° echelle with the 226-1 cross-dispersion grating, and we were able to cover 40 echelle orders with complete wavelength coverage between 6200 and 4320 Å at ~ 12 km s^{-1} spectral resolution. The price paid for this extensive wavelength coverage was a crowding of the orders near the short-wavelength end of the spectrum so that a relatively narrow decker corresponding to 6 arcsec had to be

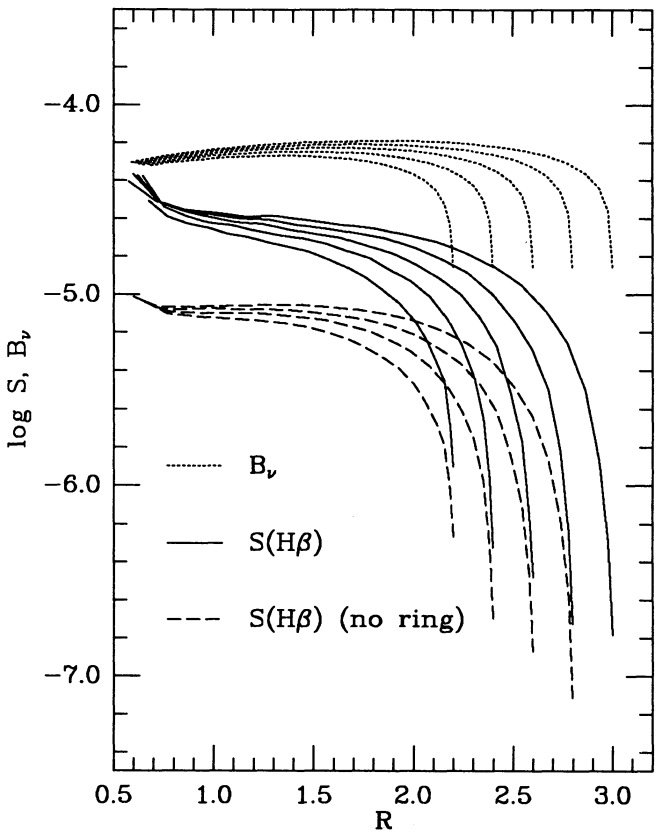

FIG. 10.—Hβ source functions used for the profiles displayed in Figs. 8 and 9, compared to the local Planck function

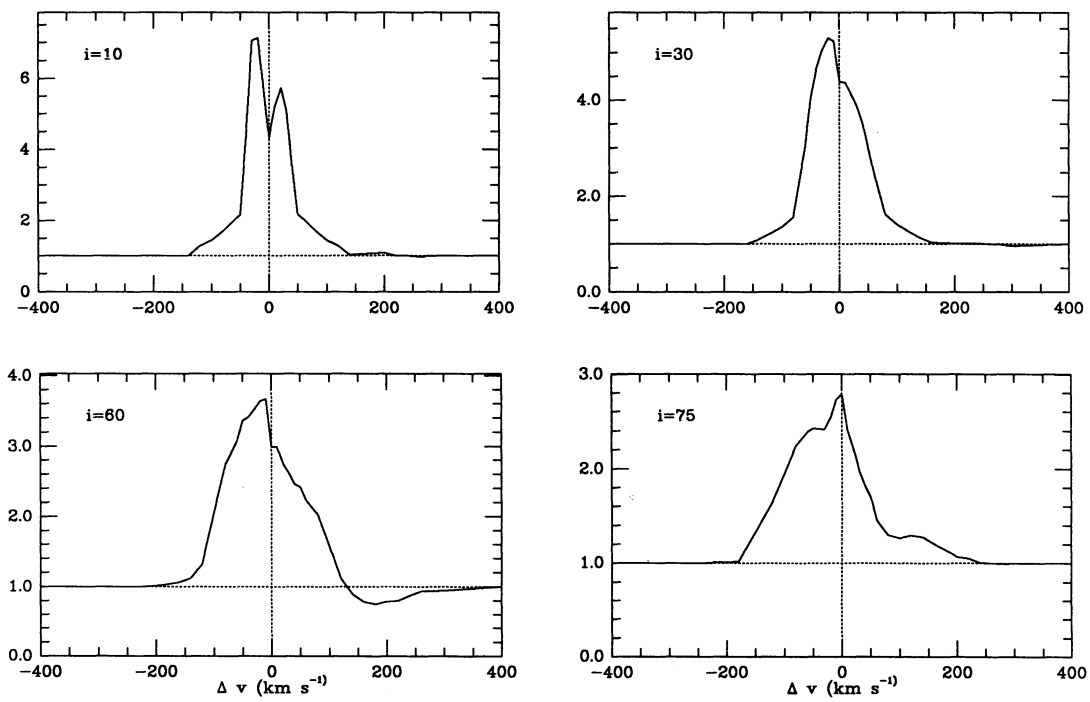

FIG. 11.—Hα line profiles for a magnetosphere with field lines intersecting the disk at $r_{mi} = 4\ R_*$ and $r_{mo} = 6\ R_*$ (see text; compare Fig. 1)

used, making it very difficult to make night sky line corrections. For the purposes of this paper, such corrections are unimportant except near the positions of the night sky lines in Na I. No interorder background corrections were attempted; it is estimated that any such corrections are $\lesssim 5\%$ of the continuum level. The data reduction was performed using standard IRAF tasks.

4.1. *BP Tau and UY Aur*

CH suggested infall models might provide better explanations of observed line profiles in general for T Tauri stars. Here we consider specific applications of the models. In Figure 12 we show the simultaneously obtained line profiles of Hβ and Hγ in BP Tau and UY Aur, compared with the nonisothermal model results for $i = 60°$. These profiles appear to be typical, based on comparison with the observations of Basri et al. (1989) and Edwards et al. (1993b). Overall, the calculations are in reasonably good agreement with the observations. Our models are limited by the uncertainty in the magnetospheric temperature distribution, and so we concentrate on qualitative properties of the line profiles. The model profiles exhibit two properties which are particularly significant:

1. *Absence of blueshifted absorption.*—One drawback of the infall model is that it cannot explain the blueshifted absorption seen in Hα. Conversely, an advantage of the infall model is that it predicts no blueshifted absorption in the higher Balmer lines. As Figure 12 shows, such absorption is often absent in T Tauri stars. On the other hand, models in which the Balmer emission arises in the wind generally predict very strong blueshifted absorption in the upper Balmer lines (see Figs. 11–15 of Hartmann et al. 1990). This absorption is very difficult to avoid in simple wind models.

2. *Central, slightly blueshifted emission peak.* In both BP Tau and UY Aur spectra the Hβ and Hγ emission is centrally peaked and slightly blueshifted with respect to the stellar rest velocity (determined previously to better than 2 km s^{-1}; Hartmann & Stauffer 1989). This is also extremely difficult to obtain with simple wind models (Figs. 11–15 in Hartmann et al. 1990). The infall model naturally predicts central emission peaks with small blueshifts.

The observations show less or no evidence for redshifted absorption in Hγ, unlike the models. However, as shown in Figures 8 and 9, the amount of redshifted absorption is sensitive to the exact geometry and to the temperature of the hot ring.

The infall model is further supported by simultaneous observations of the Na I resonance lines in BP Tau and UY Aur, which will be reported in a subsequent paper (Daugherty et al. 1994). UY Aur clearly exhibits redshifted absorption in the Na I resonance lines,

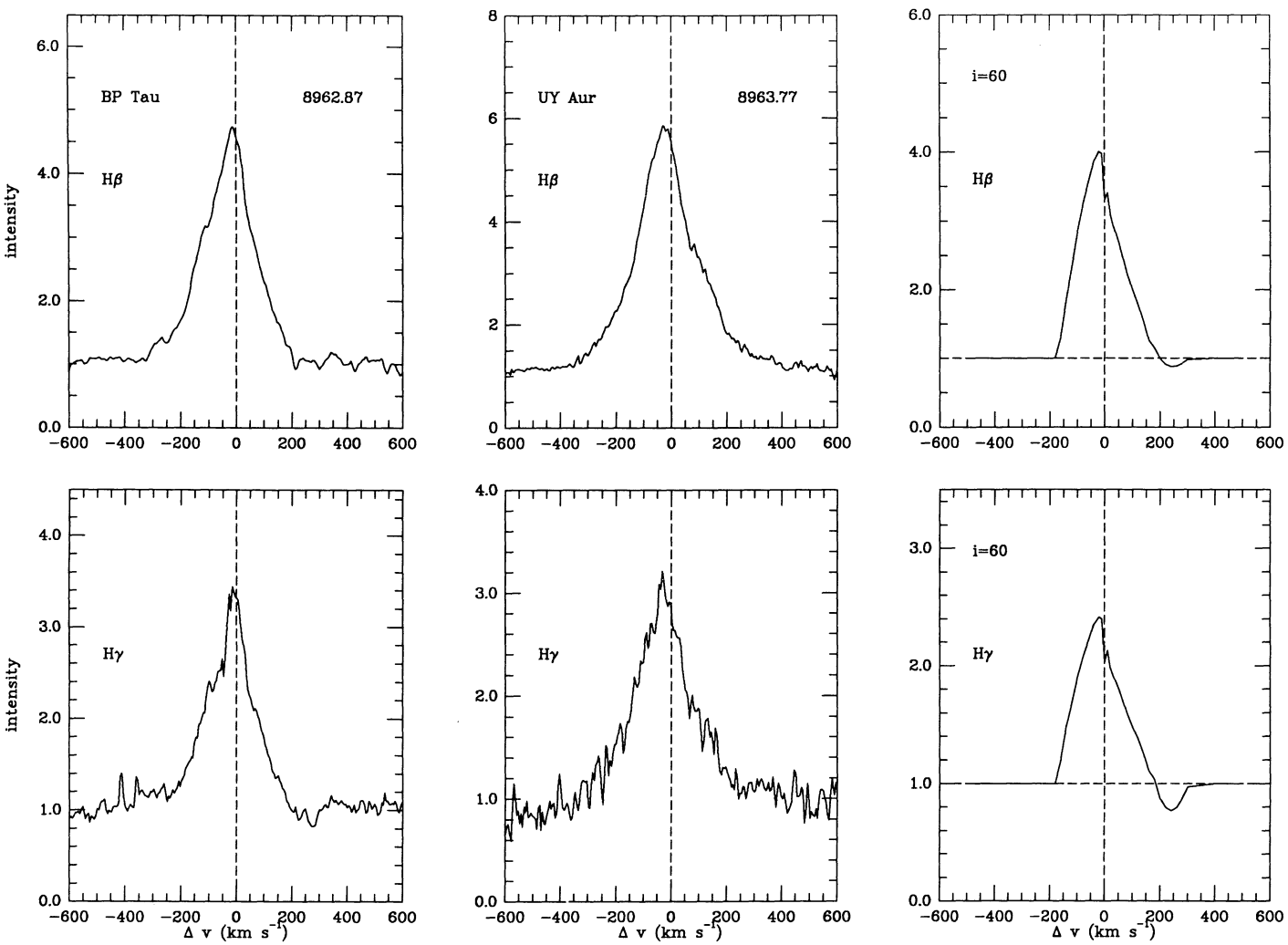

FIG. 12.—Comparison of observed Hβ and Hγ line profiles for BP Tau and UY Aur (see text) with model results from Fig. 9 with $i = 60°$

while BP Tau exhibits a slight asymmetry in the wings of the Na I lines, suggesting extra redshifted absorption. We will compare the observed Na I profiles to theoretical calculations in a subsequent paper (Daugherty et al. 1994).

4.2. *DR Tau*

The infall model line profiles cannot provide a complete explanation of T Tauri line profiles; many objects are observed to have blueshifted absorption components, which undoubtedly arise in a wind. As an example of this, we consider DR Tau, a strong-emission T Tauri star with a well-studied, intense outflow (Natta et al. 1988), but with recurring evidence for infall (Bertout et al. 1977; Krautter & Bastian 1984; Guenther & Hessman 1993).

In Figure 13 we show simultaneous Hβ, Hγ, He I, Na I, and Fe II profiles of DR Tau, along with a typical Hα profile for comparison. Strong absorption components near zero velocity and blueshifted by $\sim$180 km s^{-1} are evident in Hβ, confirming the strong wind hypothesis. Blueshifted absorption is similarly present in Hγ, but much weaker. In models which explain the emission as arising in the wind, the Hγ absorption is generally stronger than Hβ (Hartmann et al. 1990, their Figs. 11–15). A straightforward interpretation of these observations suggests that the blueshifted absorption is relatively optically thin, so that there can be a significant difference in the depths of the Hβ and Hγ absorption components due to their differing oscillator strengths. However, with such low optical depths it would be very difficult to thermalize the higher Balmer lines and produce very much emission (Hartmann et al. 1990).

Wind models also do not explain the simultaneous redshifted absorption, which is just barely discernable in Hβ, but strongly present in Hγ, just as predicted by our accretion models. The NaI lines (Fig. 13) show the blueshifted absorption of the wind, but at the same time there is an indication of redshifted absorption in the long-wavelength wing of the redmost component of the doublet, while He I λ5876 clearly shows redshifted absorption. The Fe II lines at 5018 Å (dotted line) and 4923 Å (solid line) also show inverse P Cygni structure, as well as some evidence for blueshifted absorption. (DR Tau has such strong optical continuum excess emission that its photospheric component is negligible; Hartigan et al. 1991).

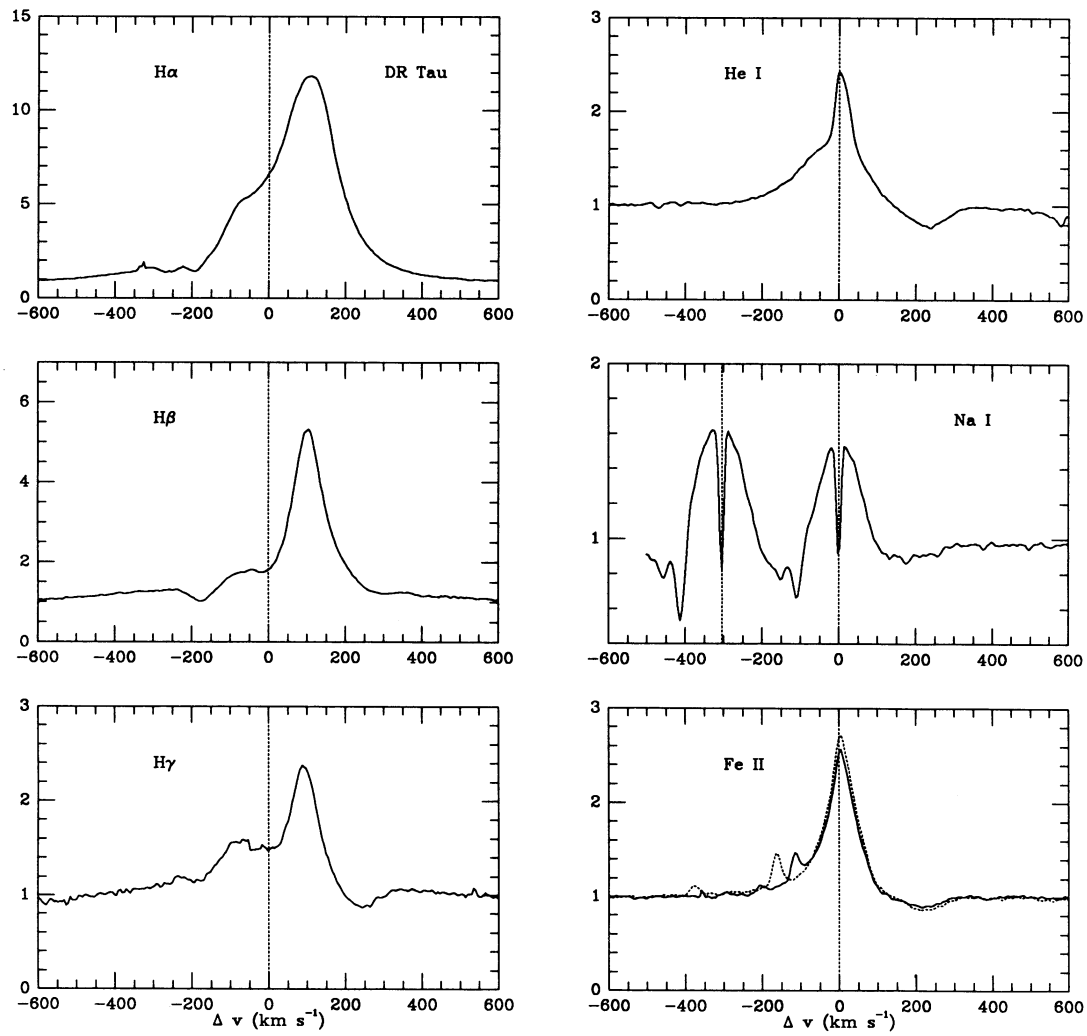

FIG. 13.—Line profiles of DR Tau. The Hβ, Hγ, Na I, He I, Fe II λ4923 (*solid line*). and Fe II λ5018 (*dotted line*) profiles were observed simultaneously. The Hα line profile was observed several years earlier and is included only for general comparison.

Thus, although the infall models cannot explain the blueshifted absorption in DR Tau, they can account for the continuing presence of redshifted absorption. The wind absorption components make it impossible to tell whether the underlying emission peak is slightly blueshifted, as in BP Tau and UY Aur. Hybrid models, composed of a magnetospheric region and a wind, will probably have to be constructed for this and similar objects (see § 5.4).

4.3. *Narrow Components*

While we have presented quantitative results only for the Balmer lines, the calculated line profiles lend themselves to two further speculations. First, the optically thin calculations suggest that infalling magnetospheric material might be at least partly responsible for the low-velocity emission seen in some forbidden lines. Often the observed [O I] profiles show two peaks; one such peak is strongly blueshifted and must originate in a stellar wind or jet (Appenzeller et al. 1984; Edwards et al. 1987), while the other tends to lie close to zero velocity. As shown in Figure 4 for the optically thin emission line, the magnetospheric material might be responsible for some emission near rest velocity. Moreover, Edwards (personal communication) has found that the low-velocity component is characterized by a higher density, at or above the high-density limit of the [S II] $\lambda\lambda$6717/6731 lines; the magnetospheric model must have very high densities. On the other hand, it is not clear that sufficiently strong emission can be produced in the magnetosphere. In our model assuming LTE, the [S II] emission would be unobservably weak. Further investigation of ionization and excitation is needed to explore this issue further.

The isothermal, optically thick line profile calculations shown in Figure 4 show a strong resemblance to some observed profiles of He I λ5876 Å. In particular, the He I line profile of DR Tau in Figure 13 is strongly reminiscent of the profile at $i = 75°$ in the right column of Figure 4; that the observed profile is produced in an infalling atmosphere is fairly evident from the obvious redshifted absorption. Modeling the excitation of He I might result in additional important constraints on magnetospheric structure. These suggestions need to be explored in models which include rotation of the magnetospheric material, an effect which could strongly affect the apparent narrowness of the central emission (Daugherty et al. 1983).

4.4. *General Predictions*

It is somewhat difficult to make detailed predictions about trends in T Tauri line profiles from the present calculations, given the possible effects of rotation, an overlying wind, and departures from axisymmetry in real stellar magnetic fields (see § 5.3). However, a few general comments can be made.

First, we confirm the suggestion of CH that Hα is much less likely to show redshifted absorption than the higher Balmer lines. In addition to the thermalization effects pointed out by CH, we also note the significance of Stark wings on Hα. In these models, with mass accretion rates $\sim 10^{-7}\ M_\odot\ \mathrm{yr}^{-1}$ and envelope temperatures $T \sim 7000$ K, we find optical depths of Hα $\sim 10^4$–10^5, which are large enough for damping wings to become important in the line profile (as well as tending to invalidate our approximate Sobolev methods). The emission damping wings of Hα will tend to obliterate any possible redshifted absorption component.

Second, in cases where line broadening due to damping or turbulence can be neglected, the extreme limits of absorption and/or emission in the P Cygni profiles should be the escape velocity of the star. This follows naturally from the gravitational cause of the motions. In contrast, wind models generally produce terminal velocities greater than the surface escape velocity. Hartmann, Edwards, & Avrett (1982) were forced to assume a restrictive damping length in their wind models for T Tauri stars to avoid excessive wind velocities.

For typical T Tauri parameters of $M = 0.8\ M_\odot$, $R = 2\ R_\odot$, the maximum infall velocity is $v(\mathrm{max} = \pm 390\ \mathrm{km\ s}^{-1}$, and given the geometrical projection effects and the requirement of a finite magnetospheric (disk truncation) radius, this upper limit should be observed rarely. If the magnetosphere structure is as in Figure 1, then there should be some tendency for line profiles to be narrow when the star is observed nearly pole-on.

Third, there is a tendency for the emission line profiles to be strongly centrally peaked and to be slightly blueshifted. This prediction will be strongly affected by the presence of any blueshifted absorption, which will tend to produce the opposing effect.

5. DISCUSSION

5.1. *Implications for T Tauri Spindown*

The magnetosphere-disk interaction model for T Tauri spin-down, based on the Ghosh & Lamb (1979a, b) theory, implies that the stellar magnetic field must couple to the disk (just) outside of the co-rotation radius r_{co}; otherwise, the star will spin up as material is accreted (Camenzind 1990; Königl 1991). For typical stellar parameters, including a typical period $P \sim 8$ days for strong-emission (accreting) T Tauri stars (Bouvier et al. 1993; Edwards et al. 1993a), the corotation radius is

$$\frac{r_{co}}{R_*} = 7.8\left(\frac{M}{0.8\ M_\odot}\right)^{1/3}\left(\frac{R_*}{2\ R_\odot}\right)^{-1}\left(\frac{P}{8\ \mathrm{days}}\right)^{2/3}. \tag{30}$$

The magnetosphere can significantly influence the disk outside of the point where free-fall begins (Livio & Pringle 1992). Thus the outer radius of our magnetospheric calculation r_{mo} does not directly constrain the angular momentum transfer, because $r_{mo} < r_{co}$ for accretion to occur. However, the existence of poloidal infall implies that the stellar magnetic field can strongly disrupt the disk, as required by the magnetospheric spindown picture, and r_{mo} is a lower limit to the radial extent of the region affected by the magnetic field.

Assuming that the adopted stellar mass and radius are approximately correct, the observed emission and absorption line shifts of ~ 200 km s^{-1} imply that $R_{out} \gtrsim 1.4\ R_*$ as a lower limit, without accounting for projection effects. By itself, this limit on R_{out} is enough to insure that T Tauri stars do not rotate at breakup. The actual value of R_{out} could easily be larger than these estimates, since infall velocities approach free-fall from infinity at larger radii. A possible limit on R_{out} may be suggested by profile calculations

including rotation. If the magnetic field in the magnetosphere is relatively stiff, as is likely, the rotational velocities of the magnetospheric material will be ~ 100 km s^{-1} out near the typical corotation radius. Such large rotation would affect the line profile significantly (e.g., Daugherty et al. 1993), and detailed comparison with observations might help place upper limits on the amount of rotation and thus on R_{out}.

5.2. *Implications for Boundary Layer Models*

Edwards et al. (1993b) find evidence for redshifted absorption in the high Balmer lines of a large fraction of classical T Tauri stars. This result, coupled with earlier indications of frequent redshifted absorption in Na I (Ulrich & Knapp 1979; Hartmann 1991) suggest that high-velocity infall is relatively common. This infall is inconsistent with the simple boundary layer model.

Our line profile results for UY Aur and BP Tau support a model in which accretion occurs in a magnetosphere extending several stellar radii above the photosphere. Although we have shown comparisons with only two objects, the evident success of the model in explaining the qualitative nature of these emission line profiles is suggestive (Fig. 12), not to mention the evidence for high-velocity infall in DR Tau (and other stars). It is difficult to believe that these T Tauri stars have sufficiently strong magnetic fields to hold off their disks to substantial distances, while many other T Tauri stars have such weak fields as to be unable to prevent boundary layer formation at distances $\lesssim 0.1\ R_*$. The implication of these results is that simple boundary layers as envisaged by Lynden-Bell & Pringle (1974) do not generally exist around T Tauri stars. The ultimate test of this hypothesis will be provided by extensive surveys of line profiles such as that of Edwards et al. (1993b).

5.3. *Detectability of Redshifted Absorption*

CH showed that the thermalization of a line could eliminate redshifted absorption in infall models and suggested that geometry could affect the visibility of redshifted absorption as well. Our results further support these contentions. The presence of a hot continuum source at the base of the accretion flow can also affect the visibility of the redshifted absorption. In contrast, the *emission* component of the line profile often exhibits a subtle, but persistent, asymmetry which may be more generally observable. In short, the absence of clear redshifted absorption does not disprove the hypothesis of infall.

5.4. *Profile Variabiliity*

"Hot spots" were originally detected due to photometric variations ascribed to the rotation of the spots across the visible stellar disk. The explanation of this phenomenon in terms of magnetically controlled accretion (Bertout et al. 1988) implies that the magnetic field is not symmetric about the stellar rotation axis. In turn, this nonaxisymmetry implies that the line profiles should be variable on the stellar rotation period even if the accretion rate is constant.

Our simple axisymmetric models cannot directly address possible profile variability; however, some general comments can be ventured. First, it seems unlikely that a dipole field model with a high angle of inclination to the rotational axis (presumably the same as the disk rotational axis) can be consistent with the observations. In such a model the accretion would occur in relatively narrow columns rather than in a ring as in the present axisymmetric model; this would seem to predict very large variations in the line profile centroid and width as the star rotates which are not evident in the observations (Basri et al. 1989).

For small variations of angle in a nearly aligned rotator, it might be possible to obtain some idea of the change in profiles by considering the results of Figures 7, 8, and 9 for changes in inclination. The models suggest that the emission-line width should vary somewhat in this case and that the equivalent width might increase as the line profile becomes narrower, but this should be verified by better calculations. One result suggested by the models is that the redshifted absorption is very sensitive to the inclination angle.

One might worry that a simple dipolar magnetic field model is inadequate to represent the stellar magnetic field, if it at all resembles the Sun's. It may be that the field close to the star is quite complex, but that the lowest order multipoles of the field tend to survive at the large distance scales required for the magnetosphere. A more detailed analysis of this problem is far beyond the scope of this paper.

5.5. *Infall and Winds*

It is evident that the magnetospheric model cannot provide a complete explanation of all T Tauri line profiles. Many stars show blueshifted absorption in strong lines which must arise in a wind. However, we argue that the *emission* generally arises in the infalling magnetospheric material, while only the blueshifted *absorption* arises in the wind. We make this argument because models which reproduce the emission line strengths of T Tauri stars require dense, optically thick envelopes (Natta et al. 1988; Hartmann et al. 1990), while the typical weakness of blueshifted absorption in high Balmer lines (e.g., Fig. 13 and § 4.2) implies a relatively low density, optically thin region.

We further speculate that the source of the wind is the disk outside of the magnetosphere, rather than a stellar wind from the magnetic pole (where field lines are not closed but open). If the wind arises from several stellar radii, the escape velocity is smaller than the escape velocity from the surface of the star. Since wind velocities generally scale with the escape velocity of the region of ejection, one might expect a relatively slow wind to result. A slow wind is needed to explain the "Type III" P Cygni profiles, in which the blueshifted absorption velocity is smaller than the velocity extent of the blueshifted emission. More work on the origins of T Tauri winds is needed to reconcile the observations of blueshifted absorption in some objects with the mounting evidence for infall.

6. CONCLUSIONS

We have presented a sequence of line profile calculations which can be used to test the magnetospheric model of T Tauri stars. A comparison of our line profile calculations with observations indicates that the strong emission lines of several T Tauri stars are

produced in infalling envelopes. Modeling the line profiles requires a stellar magnetosphere which disrupts the disk at several stellar radii. This result has two important implications. First, that T Tauri magnetospheres can be sufficiently extended that angular momentum transfer with the disk might explain the observed slow rotation (Camenzind 1990; Königl 1991). Second, a large magnetosphere implies that boundary layers are not present. The observed hot excess continuum must arise at the base of the magnetospheric accretion flow.

Although the present line profile modeling is suggestive, a number of improvements could yield more definite tests of the magnetospheric picture. Rotation must be included in the profile calculations; this will be presenteed in a forthcoming paper (Daugherty et al. 1994). It would also be helpful if a theory of the temperature structure of the infalling material could be developed. To this end, ionization and excitation calculations for other species, such as He I, using a multilevel treatment can be pursued within the framework of this model. Empirical constraints on the temperature structure could yield an improved picture of the physical processes involved, and in any event would make it possible to develop much better estimates of T Tauri mass accretion rates from the observed line profiles.

We thank S. Edwards and P. Hartigan for showing us their extensive series of T Tauri line profiles in advance of publication, and for many helpful discussions. This work was supported in part by NSF grant INT-9203015 and CONICIT grant PI-078, and by NASA grant NAGW-2919

REFERENCES

Adams, F. C., Lada, C. J., & Shu, F. H. 1987, ApJ, 312, 788
Appenzeller, I., Jankovics, I., & Ostreicher, R. 1984, A&A, 141, 108
Appenzeller, I., Mundt, R., & Wolf, B. 1978, A&A, 63, 289
Appenzeller, I., & Wolf, B. 1977, A&A, 54, 713
Basri, G., & Bertout, C. 1989, ApJ, 341, 340
Basri, G. B., Rumph, T. F., Batalha, C. C., & Stout, N. M. 1989, BAAS, 21, 716
Bastian, U. 1982, A&A, 109, 245
Bertout, C. 1977, A&A, 58, 153
———. 1979a, A&A, 80, 138
———. 1979b, Mitt. Astron. Ges., 43, 176
———. 1987, in IAU Symp. 122, Circumstellar Matter, ed. I. Appenzeller & C. Jordan (Dordrecht: Reidel), p. 23
Bertout, C., Basri, G., & Bouvier, J. 1988, ApJ, 330, 350
Bertout, C., Krautter, J., Möllenhoff, C., & Wolf, B. 1977, A&A, 61, 737
Bouvier, J., & Bertout, C. 1992, A&A, 263, 113
Bouvier, J., Cabrit, S., Fernández, M., Martin, E. L., & Matthews, J. M. 1993, A&A, 272, 176
Calvet, N., Hartmann, L., & Hewett, R. 1992, ApJ, 386, 229
Calvet, N., & Hartmann, L. 1992, ApJ, 386, 239
Camenzind, M. 1990, Reviews in Modern Astronomy (Berlin: Springer), 3, 234
Daugherty, D., et al. 1994, in preparation
Edwards, S. 1979, PASP, 91, 329
Edwards, S., Cabrit, S., Strom, S. E., Heyer, I., & Strom, K. M. 1987, ApJ, 321, 473
Edwards, S., Strom, S. E., Hartigan, P., Strom, K. M., Hillenbrand, L. A., Herbst, W., Attridge, J., Merrill, K. M., Probst, R., & Gatley, I. 1993, AJ, 106, 372
Edwards, S., et al. 1994b, in preparation
Ghosh, P., Lamb, F. K., & Pethick, C. J. 1977, ApJ, 217, 578
Guenther, E., & Hessman, F. V. 1993, A&A, in press
Hartigan, P., Hartmann, L., Kenyon, S. J., Strom, S. E., & Skrutskie, M. F. 1990, ApJ, 354, L25
Hartigan, P., Kenyon, S. J., Hartmann, L., Strom, S. E., Edwards, S., Welty, A. D., & Stauffer, J. R. 1991, ApJ, 382, 617
Hartmann, L. 1982, ApJS, 48, 109
———. 1991, in NATO ASW on Angular Momentum of Low-Mass Stars, ed. S. Catalano & J. R. Stauffer (Dordrecht: Kluwer), 379
Hartmann, L., Calvet, N., Avrett, E. H., & Loeser, R. 1990, ApJ, 349, 168
Hartmann, L., Edwards, S., & Avrett, E. H. 1982, ApJ, 259, 180
Hartmann, L., Hewett, R., Stahler, S., & Mathieu, R. D. 1986, ApJ, 309, 275
Hartmann, L., & Kenyon, S. J. 1990, ApJ, 349, 190
Hartmann, L., & MacGregor, K. B. 1980, ApJ, 242, 260
Hartmann, L., & Stauffer, J. R. 1989, AJ, 97, 873
Kenyon, S. J., & Hartmann, L. 1987, ApJ, 323, 714
Königl, A. 1991, ApJ, 370, L39
———. 1993, personal communication
Krautter, J., Appenzeller, I., & Jankovics, I. 1990, A&A, 236, 416
Krautter, J., Bastian, U. 1980, A&A, 1980, 88, L6
Lamzin, S. 1989, AZh, 66, 1329
Livio, M., & Pringle, J. E. 1992, MNRAS, 259, 23P
Lynden-Bell, D., & Pringle, J. E. 1974, MNRAS, 168, 603
Mercer-Smith, J. A., Cameron, A. G. W., & Epstein, R. I. 1984, ApJ, 279, 363
Mestel, L. 1961, MNRAS, 122, 473
Mundt, R. 1979, A&A, 74, 21
———. 1984, ApJ, 280, 749
Natta, A., Giovanardi, C., & Palla, F. 1988, ApJ, 332, 921
Osterbrock, D. E. 1974, Astrophysics of Gaseous Nebulae (San Francisco: Freeman)
Rucinski, S. 1985, AJ, 90, 2321
Rybicki, G. B., & Hummer, D. G. 1978, ApJ, 219, 654
Safier, P. 1993, ApJ, 408, 115
Scheurwater, R., & Kuijpers, J. 1988, A&A, 190, 178
Spruit, H. C., & Taam, R. E. 1990, A&A, 229, 475
Ulrich, R. K., & Knapp, G. R. 1979, ApJ, 230, L99
Vogel, S. N., & Kuhi, L. V. 1981, ApJ, 245, 960
Walker, M. F. 1972, ApJ, 175, 89
Wolf, B., Appenzeller, I., & Bertout, C. 1977, A&A, 58, 163